

# Interlaced Sparse Self-Attention for Semantic Segmentation

Lang Huang<sup>1\*</sup>, Yuhui Yuan<sup>2,3,4\*</sup>, Jianyuan Guo<sup>1</sup>, Chao Zhang<sup>1</sup>, Xilin Chen<sup>3,4</sup>, Jingdong Wang<sup>2</sup>

<sup>1</sup>Key Laboratory of Machine Perception (MOE), Peking University <sup>2</sup>Microsoft Research Asia

<sup>3</sup>Institute of Computing Technology, CAS <sup>4</sup>University of Chinese Academy of Sciences

{laynehuang, jyguo, c.zhang}@pku.edu.cn, {yuhui.yuan, jingdw}@microsoft.com, xlchen@ict.ac.cn

## Abstract

In this paper, we present a so-called interlaced sparse self-attention approach to improve the efficiency of the self-attention mechanism for semantic segmentation. The main idea is that we factorize the dense affinity matrix as the product of two sparse affinity matrices. There are two successive attention modules each estimating a sparse affinity matrix. The first attention module is used to estimate the affinities within a subset of positions that have long spatial interval distances and the second attention module is used to estimate the affinities within a subset of positions that have short spatial interval distances. These two attention modules are designed so that each position is able to receive the information from all the other positions. In contrast to the original self-attention module, our approach decreases the computation and memory complexity substantially especially when processing high-resolution feature maps. We empirically verify the effectiveness of our approach on six challenging semantic segmentation benchmarks.

## 1. Introduction

Long-range dependency plays an essential role for various computer vision tasks. The conventional deep convolutional neural networks model the long-range dependencies mainly by stacking multiple convolutions. According to the recent work [37], we need to stack nearly hundreds of consecutive  $3 \times 3$  convolutions to enable the model capturing the dependencies between any positions given the input of size  $256 \times 256$ , and we can see that the *stacking* scheme leads to very deep models that suffers from poor practical value.

The recent self-attention [41] (or non-local [44]) mechanism proposes to model the long-range dependencies through computing the context information of each output position by attending to all the input positions. We can model the dependencies between any positions in the input with a single layer equipped with self-attention mecha-

\*Equal contribution.

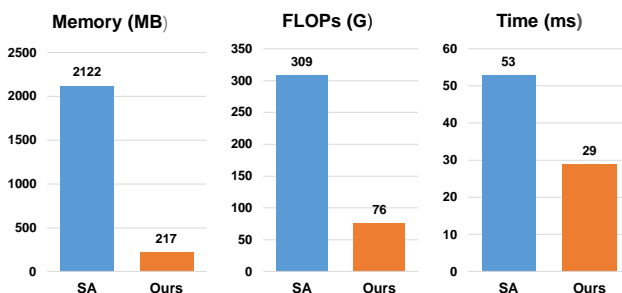


Figure 1. GPU memory/FLOPs/Time comparison between self-attention mechanism (SA) and our approach. All the numbers are tested on a single Titan XP GPU with CUDA8.0 and an input feature map of  $1 \times 512 \times 128 \times 128$  during inference stage. The lower, the better for all metrics. It can be seen that our approach only uses 10.2% GPU memory and 24.6% FLOPs while being nearly 2× faster when compared with the self-attention.

nism. The self-attention scheme has been used for various vision tasks including: video understanding [44], object detection [44], semantic segmentation [12, 53, 56] and person re-identification [23]. The computation complexity of self-attention mechanism is about  $\mathcal{O}(N^2)$  given input of size  $N$ , and the cost can become very huge for the task that requires high-resolution input such as the object detection [44] and semantic segmentation [53].

The high-resolution inputs, which are essential for high-performance in various fundamental vision tasks, take heavy computation/memory cost, preventing the potential benefit of self-attention mechanism from practical application. For example, the recent works [12, 53, 56] apply the self-attention for semantic segmentation and require more than 64 GB of GPU memory to train a model even for a small batch size such as 8. In summary, we argue that how to decrease the computation/memory cost of self-attention mechanism is of great practical value for various vision tasks that are sensitive to the computation and memory cost.

Considering that the heavy computation and memory cost mainly comes from the  $\mathcal{O}(N^2)$  complexity<sup>1</sup> of computing the dense affinity matrix  $\mathbf{A}$ , where each entry indi-

<sup>1</sup>The size of the dense affinity matrix is of size  $16384 \times 16384$  for an input feature map of spatial size  $128 \times 128$ .

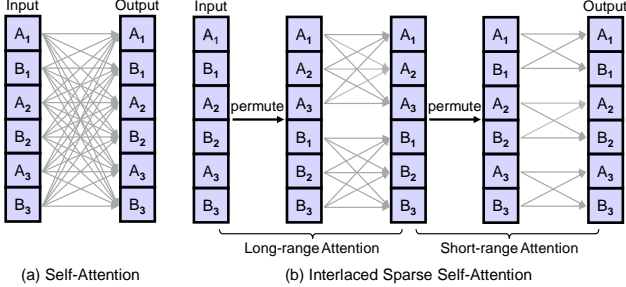


Figure 2. Information propagation path of (a) Self-Attention and (b) Interlaced Sparse Self-Attention. We use  $A_1, B_1, \dots, B_3$  to represent different positions. The gray arrows represent the information propagation path from one input position to one output position. In (a), each output position receives the propagated information from all the input positions and the connections are fully dense. In (b), we propagate the information with two steps and each step only contains very sparse connections. The first/second permute operation is used to group the positions originally have long/short spatial interval distances together.

icates the similarity between one output position and each input position. We present a simple yet efficient scheme to factorize the computation of the dense affinity matrix  $\mathbf{A}$  as the product of two sparse affinity matrices including  $\mathbf{A}^L$  and  $\mathbf{A}^S$ . In our implementation, both  $\mathbf{A}^L$  and  $\mathbf{A}^S$  are sparse block affinity matrices and their product  $\mathbf{A}^S \mathbf{A}^L$  is a dense affinity matrix. Computing these two sparse affinity matrices is much cheaper and saves large amount of cost. We theoretically show that the computation complexity of our approach is much smaller than the conventional self-attention mechanism. We illustrate the advantage of our approach over the conventional self-attention in terms of the GPU memory cost (measured by MB), computation cost (measured by GFLOPs), and inference cost (measured by ms) in Figure 1.

The implementation of our approach is inspired by the interlacing mechanism [1]. First, we divide all the input positions to  $Q$  subsets of equal size, where each set is consisted of the  $\mathcal{P}$  positions<sup>2</sup>. For the long-range attention, we sample a position from each subset to construct a new subset of  $Q$  positions, and we can construct  $\mathcal{P}$  subsets following the above sampling strategy. The positions within each constructed subset are of long spatial interval distances. We apply the self-attention on each subset to compute the sparse block affinity matrix  $\mathbf{A}^L$ . We propagate information within each sub-group according to  $\mathbf{A}^L$ . For the short-range attention, we directly apply self-attention on the original  $Q$  subsets to compute the sparse block affinity matrix  $\mathbf{A}^S$ . We then propagate information within the nearby positions according to  $\mathbf{A}^S$ . Combining these two attention mechanisms, we can propagate information from each input position to all the output positions. We have illustrated an example for our approach when processing 1-D input in Figure 2.

<sup>2</sup> $N = \mathcal{P} \times Q$ ,  $N$  is the input size.

We empirically evaluate the proposed approach on various vision tasks including semantic segmentation, object detection and instance segmentation. In summary, the contributions of this paper are summarized as below,

- We present an *interlaced sparse self-attention* scheme to capture the dense long-range dependencies more efficiently.
- We demonstrate the effectiveness of the *interlaced sparse self-attention* scheme on semantic segmentation and achieve similar or even better performance compared to the conventional self-attention mechanism.
- We empirically compare the *interlaced sparse self-attention* scheme with other mechanisms (such as CGNL [52], RCCA [16]) to illustrate the advantages of the proposed approach.

## 2. Related Work

**Self-Attention/Non-local.** The self-attention [41] is originally proposed to solve the machine translation, and the following work [44] further proposed the non-local neural network for various tasks such as video classification, object detection and instance segmentation. [15] also applies the self-attention mechanism to model the relations between the objects for better object detection. The recent [12, 53, 56] applies the similar mechanism for semantic segmentation and achieves good performance. Our work is closely related to the above works and we are mainly interested in improving the efficiency of the self-attention when processing the high-resolution input.

**CGNL/RCCA.** The recent works [52, 16, 6, 21, 19] all attempt to improve the efficiency of self-attention scheme and propose various solutions. For example, the CGNL [52] (Compact Generalized Non-local) applies the Taylor series of the RBF kernel function to approximate the pair-wise similarities, RCCA [16] (Recurrent Criss-Cross Attention) applies two consecutive criss-cross attention to approximate the original self-attention scheme and A<sup>2</sup>-Net [6] applies a set of global representations to propagate the information between all the positions more efficiently. Compared with the above works, our work is more simple and easy to implement for various tasks that originally depend on self-attention mechanism. We also empirically verify the advantages of our approach over both CGNL and RCCA.

**Interlacing/Interleaving.** The previous works have applied the interlacing mechanism for network architecture design such as the Interleaved Group Convolution [40, 47, 58], ShuffleNet [59, 31] and the Channel Local Convolution [54]. Besides, the previous space-to-channel mechanism [38, 36, 49] is also very similar to the interlacing

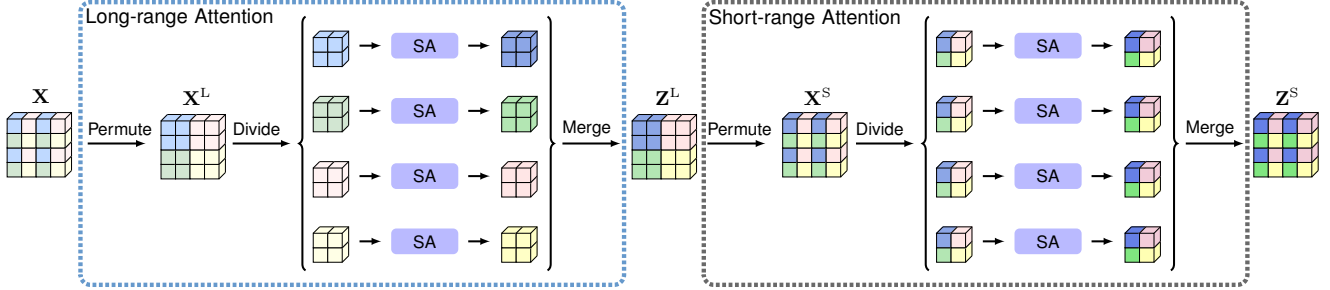


Figure 3. **Interlaced sparse self-attention.** Our approach is consisted of a long-range attention module and a short-range attention module. The feature map in the left-most/right-most is the input/output. First, we colour the input feature map  $\mathbf{X}$  with four different colors. We can see that there are 4 local groups and each group is consisted of four different colors. For the long-range attention, we permute and group (divide) all the positions with the same color having long spatial interval distances together in  $\mathbf{X}$ , which outputs  $\mathbf{X}^L$ . Then, we divide the  $\mathbf{X}^L$  to 4 groups and apply the self-attention on each group independently. We merge all the updated feature map of each group together as the output  $\mathbf{Z}^L$ . For the short range attention, we permute the  $\mathbf{Z}^L$  to group the originally nearby positions together and get  $\mathbf{X}^S$ . Then we divide and apply self-attention following the same manner as long-range attention, obtain the final feature map  $\mathbf{Z}^S$ . We can propagate the information from all the input positions to each output position with the combination of the long-range attention and the short-range attention (Best viewed in color).

mechanism. Our work is different from them as we mainly apply the interlacing mechanism to decompose the dense affinity matrix within self-attention mechanism with the product of two sparse affinity matrices, and we apply the interlacing mechanism to group the pixels with long spatial interval distances together for the long-range attention. Notably, the concurrent work Sparse Transformer [7] also applies similar factorization scheme to improve the efficiency of self-attention on sequential tasks while we are focused on semantic segmentation.

### 3. Approach

In this section, we first revisit the self-attention mechanism (Sec.3.1) and illustrate the details of the proposed interlaced sparse self-attention scheme (Sec.3.2). Last, we present the implementation of our approach with a short code based on PyTorch, which is also very easy to be implemented on other platforms (Sec.3.3).

#### 3.1. Self-Attention

The self-attention scheme is described as below,

$$\mathbf{A} = \text{Softmax}\left(\frac{\theta(\mathbf{X})\phi(\mathbf{X})^\top}{\sqrt{d}}\right), \quad (1)$$

$$\mathbf{Z} = \mathbf{A}g(\mathbf{X}), \quad (2)$$

where  $\mathbf{X}$  is the input feature map,  $\mathbf{A}$  is the dense affinity matrix, and  $\mathbf{Z}$  is the output feature map. We set their shapes as  $\mathbf{X}, \mathbf{Z} \in \mathbb{R}^{N \times C}$  and  $\mathbf{A} \in \mathbb{R}^{N \times N}$  ( $N$  is the number of pixels and  $C$  is the number of channel), and each element of  $\mathbf{A}$  records the similarities between two positions. The self-attention [41] uses two different transform functions  $\theta$  and  $\phi$  to transform the input to lower dimensional space, where  $\theta(\mathbf{X}), \phi(\mathbf{X}) \in \mathbb{R}^{N \times \frac{C}{2}}$ . The inner product on the lower dimensional space is used to compute the dense affinity ma-

trix  $\mathbf{A}$ . The scaling factor  $d$  is used to solve the small gradient problem of softmax function according to [41] and  $d = \frac{C}{2}$ . Self-attention uses the function  $g$  to learn a better embedding and  $g(\mathbf{X}) \in \mathbb{R}^{N \times C}$ .

#### 3.2. Interlaced Sparse Self-Attention

The key spirit of the proposed interlaced sparse self-attention is to decompose the dense affinity matrix in the self-attention scheme with the product of two sparse block affinity matrices including  $\mathbf{A}^L$  and  $\mathbf{A}^S$ . We illustrate how to estimate the  $\mathbf{A}^L$  with the long-range attention and the  $\mathbf{A}^S$  with the short-range attention. With the combination of the long-range attention and the short-range attention, we can propagate information from all the input positions to each output position. We illustrate our approach with an example in Figure 3.

**Long-range Attention.** The main point of the long-range attention is to apply the self-attention on the subsets of positions that have long spatial interval distances.

As illustrated in Figure 3, we first apply a permutation on the input feature map  $\mathbf{X}$  to compute  $\mathbf{X}^L = \text{Permute}(\mathbf{X})$ . Then, we divide the  $\mathbf{X}^L$  into  $\mathcal{P}$  partitions and each partition contains  $\mathcal{Q}$  neighboring positions ( $N = \mathcal{P} \times \mathcal{Q}$ ) following:  $\mathbf{X}^L = [\mathbf{X}_1^L, \mathbf{X}_2^L, \dots, \mathbf{X}_p^L]^\top$ , where each  $\mathbf{X}_p^L$  is a subset of  $\mathbf{X}^L$  and its shape is  $\mathbb{R}^{\mathcal{Q} \times C}$ . We apply the self-attention on each  $\mathbf{X}_p^L$  independently as below,

$$\mathbf{A}_p^L = \text{Softmax}\left(\frac{\theta(\mathbf{X}_p^L)\phi(\mathbf{X}_p^L)^\top}{\sqrt{d}}\right), \quad (3)$$

$$\mathbf{Z}_p^L = \mathbf{A}_p^L g(\mathbf{X}_p^L), \quad (4)$$

where  $\mathbf{A}_p^L \in \mathbb{R}^{\mathcal{Q} \times \mathcal{Q}}$  is a small affinity matrix based on all the positions from  $\mathbf{X}_p^L$  and  $\mathbf{Z}_p^L \in \mathbb{R}^{\mathcal{Q} \times C}$  is the updated representation based on  $\mathbf{X}_p^L$ . All the other choices including  $d$ ,  $\theta$ ,  $\phi$  and  $g$  are the same as the self-attention scheme.

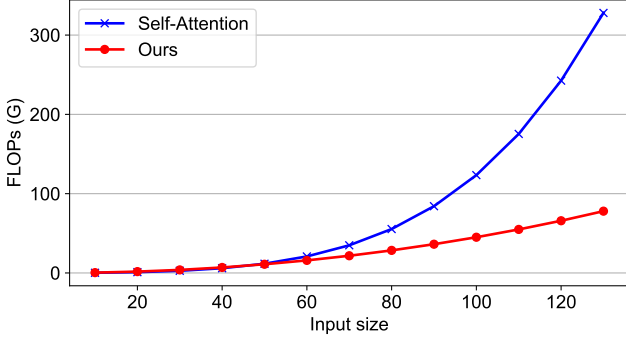


Figure 4. **FLOPs vs. input size.** The  $x$ -axis represents the height or width of the input feature map (we assume the height is equal to the width for convenience) and the  $y$ -axis represents the computation cost measured with GFLOPs. It can be seen the GFLOPs of self-attention mechanism increases much faster than our approach with higher resolution inputs.

Last, we merge all the  $\mathbf{Z}_p^L$  from different groups and get the output  $\mathbf{Z}^L = [\mathbf{Z}_1^{L\top}, \mathbf{Z}_2^{L\top}, \dots, \mathbf{Z}_p^{L\top}]^\top$ . We illustrate the actual affinity matrix of the long-range attention  $\mathbf{A}^L$  as below,

$$\mathbf{A}^L = \begin{bmatrix} \mathbf{A}_1^L & 0 & \dots & 0 \\ 0 & \mathbf{A}_2^L & \dots & 0 \\ \vdots & \vdots & \ddots & \vdots \\ 0 & 0 & \dots & \mathbf{A}_p^L \end{bmatrix}, \quad (5)$$

where we can see that only the affinity values in the diagonal blocks are non-zero. We can also use  $\mathbf{A}^L = \text{diag}(\mathbf{A}_1^L, \mathbf{A}_2^L, \dots, \mathbf{A}_p^L)$  to represent the sparse block matrix for convenience.

**Short-range Attention.** The main point of the short-range attention is to apply the self-attention on the subsets of positions that have short spatial interval distances.

According to Figure 3, we apply another permutation on the output feature map from the long-range attention following  $\mathbf{X}^S = \text{Permute}(\mathbf{Z}^L)$ . Then, we divide  $\mathbf{X}^S$  into  $\mathcal{Q}$  partitions and each partition contains  $\mathcal{P}$  neighboring positions following:  $\mathbf{X}^S = [\mathbf{X}_1^{S\top}, \mathbf{X}_2^{S\top}, \dots, \mathbf{X}_Q^{S\top}]^\top$ , where each  $\mathbf{X}_q^S$  is of size  $\mathbb{R}^{\mathcal{P} \times C}$ . We apply the self-attention on each  $\mathbf{X}_q^S$  independently, which is similar with the Equation 3 and Equation 4 in the long-range attention. Accordingly, we can get  $\mathbf{A}_q^S$  and  $\mathbf{Z}_q^S$ , where  $\mathbf{A}_q^S \in \mathbb{R}^{\mathcal{P} \times \mathcal{P}}$  is a small affinity matrix based on  $\mathbf{X}_q^S$ ,  $\mathbf{Z}_q^S \in \mathbb{R}^{\mathcal{P} \times C}$  is the updated representation based on  $\mathbf{X}_q^S$ .

Last, we merge all the updated representation as  $\mathbf{Z}^S = [\mathbf{Z}_1^{S\top}, \mathbf{Z}_2^{S\top}, \dots, \mathbf{Z}_Q^{S\top}]^\top$ . The sparse block affinity for the short-range attention is illustrated as below,

$$\mathbf{A}^S = \text{diag}(\mathbf{A}_1^S, \mathbf{A}_2^S, \dots, \mathbf{A}_Q^S), \quad (6)$$

where we can see that the actual affinity matrix  $\mathbf{A}^S$  for the short-range attention is also very sparse and most of the affinity values are zero.

```
def InterlacedSparseSelfAttention(x, P_h, P_w):
    # x: input features with shape [N,C,H,W]
    # P_h, P_w: Number of partitions along H and W dimension

    N, C, H, W = x.size()
    Q_h, Q_w = H // P_h, W // P_w
    x = x.reshape(N, C, Q_h, P_h, Q_w, P_w)

    # Long-range Attention
    x = x.permute(0, 3, 5, 1, 2, 4)
    x = x.reshape(N * P_h * P_w, C, Q_h, Q_w)
    x = SelfAttention(x)
    x = x.reshape(N, P_h, P_w, C, Q_h, Q_w)

    # Short-range Attention
    x = x.permute(0, 4, 5, 3, 1, 2)
    x = x.reshape(N * Q_h * Q_w, C, P_h, P_w)
    x = SelfAttention(x)
    x = x.reshape(N, Q_h, Q_w, C, P_h, P_w)

    return x.permute(0, 3, 1, 4, 2, 5).reshape(N, C, H, W)
```

Figure 5. Python code of our approach based on PyTorch.

Finally, we directly fuse the output  $\mathbf{Z}^S$  from the short-range attention and the input feature map  $\mathbf{X}$  following the previous works [44, 53]. Especially, all of our above analysis can be generalized to higher dimensional inputs easily.

**Complexity.** Given an input feature map of size  $H \times W \times C$ , we analyze the computation / memory cost of both the self-attention mechanism and our approach.

The complexity of self-attention mechanism is  $\mathcal{O}(2HWC^2 + \frac{3}{2}(HW)^2C)$ . And the complexity of our approach is  $\mathcal{O}(4HWC^2 + \frac{3}{2}(HW)^2C(\frac{1}{\mathcal{P}_h\mathcal{P}_w} + \frac{1}{\mathcal{Q}_h\mathcal{Q}_w}))$ , where we divide the height dimension to  $\mathcal{P}_h$  groups and the width dimension to  $\mathcal{P}_w$  groups in the long-range attention and  $\mathcal{Q}_h$  and  $\mathcal{Q}_w$  groups during the short-range attention, and  $H = \mathcal{P}_h\mathcal{Q}_h$ ,  $W = \mathcal{P}_w\mathcal{Q}_w$ . The complexity of our approach can be minimized to  $\mathcal{O}(4HWC^2 + 3(HW)^{\frac{3}{2}}C)$  when  $\mathcal{P}_h\mathcal{P}_w = \sqrt{HW}$ . We compare the numerical complexity of our approach and the self-attention in Figure 4. It can be seen that our approach is much more efficient than the conventional self-attention when processing inputs of high resolution.

### 3.3. Implementation

Our approach can be easily implemented with a few lines of code in Python. We show the code of our approach in 5 based on PyTorch. For the self-attention operation, we directly use the open-source implementation from [53]. As illustrated in Figure 5, we implement the Permutation and Divide operation in the long-range attention / short-range attention by calling the default permute and reshape functions. Besides, we implement all the transform functions including  $\theta$ ,  $\phi$  and  $g$  with  $1 \times 1$  convolution + BN + ReLU. The output channels of  $\theta$  function and  $\phi$  function are set as half of the input channels, whereas the output channel of  $g(\cdot)$  remains the same as the input channels. Following [41, 44, 53], we fuse the input feature map and the fea-



ture map output from our interlaced sparse self-attention via residual connection or concatenation.

## 4. Experiments

We first compare our approach with the recent state-of-the-art on six challenging semantic segmentation benchmarks including: Cityscapes [8], ADE20K [62], LIP [20], PASCAL VOC 2012 [11], PASCAL-Context [33] and COCO-Stuff [2]. Then we study the application of our method to the Mask R-CNN baseline [14] on the object detection and instance segmentation benchmark COCO [26]. Finally, we conduct extensive ablation studies on our approach.

### 4.1. Semantic Segmentation

We first illustrate the details of all six benchmarks, and then we provide the related results on each benchmark. Especially, we use mIoU (mean of class-wise intersection over union) and pixel accuracy as evaluation metrics on all six semantic segmentation benchmarks.

**Cityscapes.** The dataset contains 5,000 finely annotated images with 19 semantic classes. The images are in  $2048 \times 1024$  resolution and captured from 50 different cities. The training, validation, and test sets consist of 2,975, 500, 1,525 images respectively.

**ADE20K.** The dataset is very challenging that contains 22K densely annotated images with 150 fine-grained semantic concepts. The training and validation sets consist of 20K, 2K images respectively.

**LIP.** The dataset is a large-scale dataset that focuses on semantic understanding of human bodies. It contains 50K images with 19 semantic human part labels and 1 background label for human parsing. The training, validation, and test sets consist of 30K, 10K, 10K images respectively.

**PASCAL VOC 2012.** The dataset is a conventional object-centric segmentation dataset. It contains more than 13K images with 20 object labels and 1 background label. The training, validation and test sets consist of about 10K, 1K and 1K images respectively.

**PASCAL-Context.** The dataset is a scene parsing dataset that contains 59 semantic classes and 1 background class. The training and validation set consist of about 5K and 5K images respectively.

**COCO-Stuff.** The dataset is a very challenging segmentation dataset that involves 80 object classes and 91 stuff classes. The training and validation set consist of 9K and 1K images respectively.

**Network.** We use ImageNet-pretrained ResNet-50/ResNet-101 as our backbone [29]. Following the common practice [5], we remove the last two down-sample operation

in the ResNet-50/ResNet-101 and employ dilated convolutions in last two stages, thus the size of the output feature map is  $8 \times$  smaller than input image. Following [53, 12], we reduce the number of channels of the output feature map to 512 with a  $3 \times 3$  convolution. Then we apply interlaced sparse self-attention module on the reduced feature map and obtain a feature map  $\mathbf{Z}$  of size  $512 \times H \times W$ . We directly predict (and upsample) the segmentation map based on  $\mathbf{Z}$ .

**Training setting.** For all the six semantic segmentation benchmarks, we use the "poly" learning rate policy where the learning rate is multiplied by  $(1 - (\frac{iter}{iter_{max}})^{power})$  with power as 0.9. We choose momentum of 0.9 and a weight decay of 0.0005. Besides, we also apply an auxiliary loss on the intermediate feature map after res-4 stage of ResNet with a weight of 0.4 following the PSPNet [60]. For the data augmentation, we apply random horizontal flip, random scaling (from 0.5 to 2.0) and random crop over all the training images. Especially, we use the synchronized batch normalization [35] in all of our experiments. We use  $4 \times P100$  GPUs for the training of all of our experiments.

We adopt different initial learning rates, batch sizes and training epochs by following the previous works. For Cityscapes, we choose initial learning rate of 0.01, batch size of 8 and crop size of  $769 \times 769$  [5, 60]. For ADE20K, we choose initial learning rate of 0.02, batch size of 16 and crop size of  $520 \times 520$  following [60, 53]. For LIP, we choose initial learning rate of 0.007, batch size of 40 and crop size of  $473 \times 473$  following [27]. For PASCAL VOC 2012 and PASCAL-Context, we choose initial learning rate of 0.01, batch size of 16 and crop size of  $513 \times 513$  following [4, 55]. For COCO-Stuff, we choose initial learning rate of 0.01, batch size of 16 and crop size of  $520 \times 520$ . We train the models for 110 epochs on Cityscapes, 120 epochs on ADE20K, 150 on LIP, 80 epochs on PASCAL VOC 2012, PASCAL-Context and 100 epochs on COCO-Stuff.

**Results on Cityscapes.** We report the results in Table 1 to compare our approach with the recent state-of-the-arts on the test set of Cityscapes, where we apply the multi-scale testing and flip testing following the previous works. Our approach outperforms most of other approaches when only using the fine datasets for training. For example, our approach achieves 80.3% and outperforms the previous AAF [17] by 1.2%. Compared with DANet [12] (based on channel self-attention and spatial self-attention), our approach requires much smaller computation cost according to the complexity comparison in Table 13.

**Results on ADE20K.** In Table 2, we compare our approach with the state-of-the-arts on the validation set of ADE20K. For fair comparison, we employ ResNet-101 backbone and multi-scale testing following other methods. From the results, we can see that our approach achieves better performance compared to all other methods. For example, our

Table 1. Comparison with state-of-the-arts on the test set of Cityscapes. We report both results trained with and without validation set.

Method	Backbone	Validation set	mIoU (%)
PSPNet [60]	ResNet-101	✗	78.4
PSANet [61]	ResNet-101	✗	78.6
AAF [17]	ResNet-101	✗	79.1
RefineNet [24]	ResNet-101	✓	73.6
DUC-HDC [43]	ResNet-101	✓	77.6
DSSPN [22]	ResNet-101	✓	77.8
SAC [57]	ResNet-101	✓	78.1
DepthSeg [18]	ResNet-101	✓	78.2
BiSeNet [50]	ResNet-101	✓	78.9
DFN [51]	ResNet-101	✓	79.3
TKCN [45]	ResNet-101	✓	79.5
PSANet [61]	ResNet-101	✓	80.1
DenseASPP [48]	DenseNet-161	✓	80.6
SVCNet [10]	ResNet-101	✓	81.0
DANet [12]	ResNet-101	✓	<b>81.5</b>
Ours	ResNet-101	✗	80.3
Ours	ResNet-101	✓	<u>81.4</u>

Table 2. Comparison with state-of-the-arts on the validation set of ADE20K.

Method	Backbone	mIoU (%)
RefineNet [24]	ResNet-101	40.20
RefineNet [24]	ResNet-152	40.70
UperNet [46]	ResNet-101	42.66
PSPNet [60]	ResNet-101	43.29
PSPNet [60]	ResNet-152	43.51
DSSPN [22]	ResNet-101	43.68
PSANet [61]	ResNet-101	43.77
SAC [57]	ResNet-101	44.30
SGR [21]	ResNet-101	44.32
EncNet [55]	ResNet-101	44.65
GCU [19]	ResNet-101	<u>44.81</u>
Ours	ResNet-101	<b>45.04</b>

approach achieves 45.04% mIoU, which improves the recent GCU [19] that using the same backbone by 0.2%. Especially, improving 0.2% is not neglectable considering the improvements on ADE20K is very challenging.

**Results on LIP.** We compare our approach to the previous state-of-the-arts on LIP and illustrate the results in Table 3. According to the results, it can be seen that our approach achieves new state-of-the-art performance 55.07%, which outperforms all the other methods using the same backbone by a large margin. Notably, we only employ single scale testing following CE2P [27] and multi-scale testing can be further incorporated to improve performance.

**Results on PASCAL VOC 2012.** The PASCAL VOC 2012 dataset is one of gold standard benchmarks for semantic segmentation. Following [55, 5], we first train the model on the *trainaug* set and then finetuned the model on the *trainval* set. As reported in Table 4, we achieve 83.2% mIoU on

Table 3. Comparison with state-of-the-arts on the validation dataset of LIP.

Method	Backbone	mIoU (%)
Attention+SSL [13]	ResNet-101	44.73
MMAN [30]	ResNet-101	46.81
SS-NAN [57]	ResNet-101	47.92
MuLA [34]	ResNet-101	49.30
JPPNet [20]	ResNet-101	51.37
CE2P [27]	ResNet-101	<u>53.10</u>
Ours	ResNet-101	<b>55.07</b>

Table 4. Comparison with state-of-the-arts on the test set of PASCAL VOC 2012 (w/o COCO data).

Method	Backbone	mIoU (%)
FCN [29]	VGG-16	62.2
DeepLab-CRF [3]	VGG-16	71.6
DPN [28]	DPN	74.1
PSPNet [60]	ResNet-101	82.6
DFN [51]	ResNet-101	82.7
EncNet [55]	ResNet-101	<u>82.9</u>
DANet [12]	ResNet-101	82.6
Ours	ResNet-101	<b>83.2</b>

Table 5. Comparison with state-of-the-arts on the validation set of PASCAL-Context. mIoU is evaluated on 60 classes w/ background.

Method	Backbone	mIoU (%)
DeepLabv2 [4]	ResNet-101	45.7
UNet++ [63]	ResNet-101	47.7
PSPNet [60]	ResNet-101	47.8
CCL [9]	ResNet-101	51.6
EncNet [55]	ResNet-101	51.7
DANet [12]	ResNet-101	52.6
SVCNet [10]	ResNet-101	<u>53.2</u>
Ours	ResNet-101	<b>54.1</b>

the PASCAL VOC 2012 test set and slightly outperforms the DANet while being much more efficient.

**Results on PASCAL-Context.** As illustrated in Table 5, we compare our approach with the previous state-of-the-arts on the validation set of PASCAL-Context. Our approach achieves 54.1% mIoU and outperforms all the other approaches.

**Results on COCO-Stuff.** We further compare our method with the previous state-of-the-arts on the validation set of COCO-Stuff benchmark. According to the results illustrated in Table 6, our method also achieves competitive performance while being more efficient than the conventional self-attention based approaches.

## 4.2. Application to Mask-RCNN

**Dataset.** We use COCO [26] dataset to evaluate our approach. The dataset is one of the most challenging datasets for object detection and instance segmentation, which con-

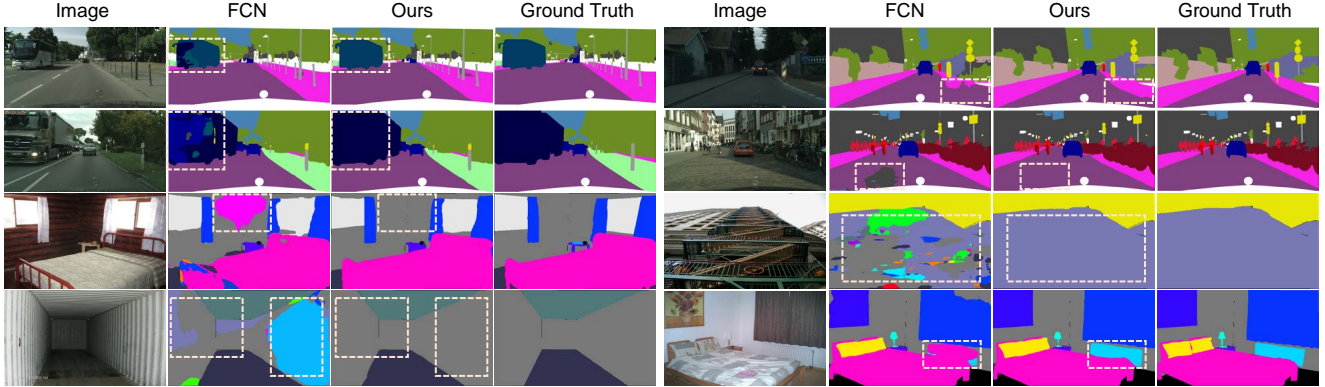


Figure 6. Visual improvements of our approach over the baseline on both Cityscapes (first two rows) and ADE20K (last two rows). We mark the improved regions with white dashed boxes (Best viewed in color).

Table 6. Comparison with state-of-the-arts on the validation set of COCO-Stuff.

Method	Backbone	mIoU (%)
FCN [29]	VGG-16	22.7
DAG-RNN [39]	VGG-16	31.2
RefineNet [24]	ResNet-101	33.6
CCL [9]	ResNet-101	35.7
SVCNet [10]	ResNet-101	39.6
DANet [12]	ResNet-101	<b>39.7</b>
Ours	ResNet-101	39.2

tains 140K images annotated with object bounding boxes and masks of 80 categories. We follow the COCO2017 split as in [14], where the training, validation and test sets contains 115K, 5K, 20K images respectively. We report the standard COCO metrics including Average Precision (AP),  $AP_{50}$  and  $AP_{75}$  for both bounding boxes and masks.

**Training settings.** We use Mask-RCNN [14] as baseline to conduct our experiments. Similar to [44], we insert 1 non-local or interlaced sparse self-attention block before the last block of res-4 stage of the ResNet-50 FPN [25] backbone. All models are initialized with ImageNet pretrained weights and built upon open source toolbox [32]. We train the models using SGD with batch size of 16 and weight decay of 0.0001. We conduct experiments using training schedules including ‘1× schedule’ and ‘2× schedule’ [32]. The 1× schedule starts at a learning rate of 0.02 and is decreased by a factor of 10 after 60K and 80K iterations and finally terminates at 90K iterations. We train for 180K iterations for 2× schedule and decreases the learning rate proportionally. The other training and inference strategies keep the same with the default settings in the [32].

**Results.** We report the results on COCO dataset in Table 7. We can see that adding one non-local block [44] or interlaced sparse self-attention module consistently improves the Mask-RCNN baseline by  $\sim 1\%$  on all metrics

Table 7. Comparison with non-local [44] (NL) on the validation set of COCO. We use Mask-RCNN [14] as baseline and employ ResNet-50 FPN backbone for all models.

Method	Schedule	$AP^{box}$	$AP_{50}^{box}$	$AP_{75}^{box}$	$AP^{mask}$	$AP_{50}^{mask}$	$AP_{75}^{mask}$
Mask-RCNN	1×	37.7	59.2	41.0	34.2	56.0	36.2
+ NL	1×	<b>38.8</b>	60.6	42.3	35.1	<b>57.4</b>	37.3
+ Ours	1×	<b>38.8</b>	<b>60.7</b>	<b>42.5</b>	<b>35.2</b>	57.3	<b>37.6</b>
Mask-RCNN	2×	38.7	59.9	42.1	34.9	56.8	37.0
+ NL	2×	<b>39.7</b>	<b>61.3</b>	<b>43.4</b>	<b>35.9</b>	<b>58.3</b>	<b>38.2</b>
+ Ours	2×	<b>39.7</b>	61.1	43.3	35.7	57.8	38.1

Table 8. Influence of  $\mathcal{P}_h$  and  $\mathcal{P}_w$  within the interlaced sparse self-attention on the validation set of Cityscapes.

Method	$\mathcal{P}_h$	$\mathcal{P}_w$	Pixel Acc (%)	mIoU (%)
Baseline	-	-	96.08	75.90
+ Ours	4	4	96.30	78.97
	4	8	96.31	78.95
	8	4	96.32	79.31
	8	8	<b>96.33</b>	<b>79.49</b>
	8	16	96.29	79.04
	16	8	96.19	78.90
	16	16	96.32	79.40

involving both object detection and instance segmentation. Similar gains are observed for both 1× schedule and 2× schedule. For example, our approach improves the box AP/mask AP of Mask-RCNN from 38.7/34.9 to 39.7/35.7 with 2× schedule. Especially, the performance of our approach is comparable with the non-local block on all metrics while decreasing the computation complexity significantly.

### 4.3. Ablation Study

**Influence of the partition numbers.** We investigate the influence of the partition numbers of our approach, e.g.,  $\mathcal{P}$ ,  $\mathcal{Q}$ . We conduct the experiments with various choices of  $\mathcal{P}$  and  $\mathcal{Q}$ , and present the related results in Table 8. Especially, we can determine the value of  $\mathcal{Q}_h$  and  $\mathcal{Q}_w$  according to  $\mathcal{P}_h$  and  $\mathcal{P}_w$ . According to the results in Table 8, it can be seen that our approach consistently improves over the baseline under



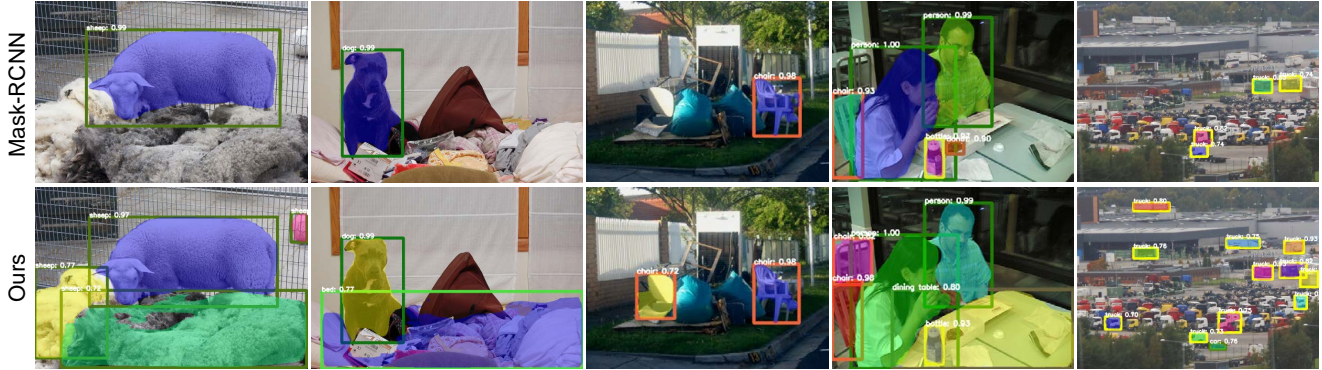


Figure 7. Visualization of the object detection and instance segmentation results of Mask-RCNN [14] and our approach on the validation set of COCO (Best viewed in color).

Table 9. Impact of the order of long-range and short-range attention on the validation set of Cityscapes.

Method	Pixel Acc (%)	mIoU (%)
Baseline	96.08	75.90
+ Ours (Short + Long)	96.26	79.10
+ Ours (Long + Short)	<b>96.33</b>	<b>79.49</b>

various choices of the hyper-parameters. And the choice  $\mathcal{P}_h = \mathcal{P}_w = 8$  achieves slightly better results than others. We simply set  $\mathcal{P}_h = \mathcal{P}_w = 8$  for all of our experiments for convenience. All the above experiments use the ResNet-101 FCN as the backbone and use the same training and testing settings.

**Long+Short vs. Short+Long.** Considering that we can achieve the fully dense information propagation with either long-range attention first or short-range attention first, we study the influence of the order of the long-range attention and the short-range attention on the semantic segmentation task. We simply conduct another group of experiments to firstly apply the short-range attention and then the long-range-attention. The related results are summarized in Table 9. It can be seen that changing the order still improves over the baseline for a large margin. Applying the long-range attention firstly seems to be preferred for the semantic segmentation tasks. We use the ResNet-101 FCN as the backbone for all the above experiments. In all of our experiments, we apply the long-range attention firstly unless otherwise specified.

**Comparison with Self-Attention/Non-local.** We compare our approach with the self-attention/non-local mechanism on three semantic segmentation datasets. We report the related results in Table 10. We use ResNet-50 as the backbone for experiments on ADE20K and ResNet-101 as the backbone for all the other experiments. We can see that our approach outperforms the self-attention on all three datasets. For example, our approach outperforms the self-attention based approach by 0.56%/0.96%/0.84% on ADE20K/Cityscapes/LIP respectively.

Table 10. Comparison with self-attention (SA) and Pyramid Pooling Module (PPM) on three datasets. We use CE2P [27] as our baseline for LIP and ResNet based FCN for Cityscapes and ADE20K.

Method	Dataset	Backbone	Pixel Acc (%)	mIoU (%)
Baseline	ADE20K	ResNet-50	76.41	34.35
+ PPM			80.17	41.50
+ SA			80.19	41.55
+ Ours			<b>80.27</b>	<b>42.11</b>
Baseline	Cityscapes	ResNet-101	96.08	75.90
+ PPM			96.20	78.50
+ SA			96.21	78.53
+ Ours			<b>96.33</b>	<b>79.49</b>
CE2P	LIP	ResNet-101	87.37	53.10
+ PPM			87.21	54.18
+ SA			87.23	54.23
+ Ours			<b>87.69</b>	<b>55.07</b>

**Comparison with Pyramid Pooling Module.** We also compare our approach with the well verified Pyramid Pooling Module (PPM) [60] under the same training/testing settings. We report the related results in Table 10. We can see that our approach consistently outperforms the PPM on all three datasets. Specifically, our approach outperforms the PPM by 0.61%/0.99%/0.89% on ADE20K/Cityscapes/LIP respectively. In fact, the advantage of self-attention over PPM has also been convincingly verified in the previous works including DANet [12], CFNet [56], and OCNet [53]. The (further) advantage of our approach compared with [12, 56, 53] is the significant efficiency improvement.

**Comparison with CGNL.** The recently proposed compact generalized non-local module (CGNL) [52] also attempts to improve the efficiency of the original non-local mechanism. Considering the CGNL is extensively evaluated on the fine-grained classification dataset, we compare our approach with CGNL on CUB-200-2011 [42] dataset.

We use ResNet-50 as backbone to for all the experiments. Following [44, 52], we compare our approach with



Table 11. Comparison with CGNL [52] on the validation set of CUB-200-2011.

Method	Top1 Acc (%)	Top5 Acc (%)
ResNet-50	84.37	96.53
+ 1× CGNL [52]	85.14	96.88
+ 5× CGNL [52]	85.68	96.69
+ 1× CGNL (Our impl.)	85.69	96.95
+ 5× CGNL (Our impl.)	86.31	97.05
+ 1× Ours	86.28	97.03
+ 5× Ours	<b>86.54</b>	<b>97.10</b>

Table 12. Comparison with SA [41] with 2× downsampling, RCCA [16] and CGNL [52] on the validation set of Cityscapes. All methods choose ResNet-101 FCN as the backbone.

Method	Pixel Acc (%)	mIoU (%)
Baseline	96.08	75.90
+ RCCA [16]	-	79.12
+ SA-2× (Our impl.)	96.12	76.49
+ RCCA (Our impl.)	96.28	78.63
+ CGNL (Our impl.)	96.01	77.01
+ Ours	<b>96.33</b>	<b>79.49</b>

CGNL under two different settings: (1) insert one CGNL or interlaced sparse self-attention module (to res-4); (2) insert 5 CGNL or interlaced sparse self-attention modules (2 modules to res-3 and 3 modules to res-4). We report the Top-1 and Top-5 classification accuracy on the validation set of CUB-200-2011 in Table 11. It can be seen that our approach outperforms the previous CGNL under both kinds of settings. Besides, we also verify the advantages of our approach over CGNL on a segmentation dataset (Cityscapes) and illustrate the performance in Table 12.

**Comparison with Down-Sampling/RCCA.** We compare our approach with other two kinds of mechanisms that are conventionally used to improve the efficiency of self-attention/non-local such as the down-sampling scheme [44] and RCCA [16]. For the down-sampling scheme, we directly down-sample the feature map for 2× before computing the dense affinity matrix. We evaluate both kinds of mechanisms on the validation set of Cityscapes and report the related performance in Table 12. It can be seen that our approach outperforms the above two mechanisms according to the results in Table 12. Especially, we use the average performance (79.12%) reported in [16] for fairness.

**Efficiency Comparison.** We compare our approach with PPM [60], SA [41], DANet [12], RCCA [16] and CGNL [52] in terms of efficiency in this section. We report the GPU memory, GFLOPs and inference time when processing input feature map of size  $2048 \times 128 \times 128$  in Table 13. It can be seen that our approach is much more efficient than all the other approaches.

**Visualization.** First, we visualize the segmentation maps

Table 13. Efficiency comparison given input feature map of size  $[2048 \times 128 \times 128]$  in inference stage.

Method	Memory (MB)	GFLOPs	Time (ms)
PPM [60]	664	619	75
SA [41]	2168	619	77
DANet [12]	2339	1110	121
RCCA [16]	427	804	131
CGNL [52]	266	412	75
Ours	<b>252</b>	<b>386</b>	<b>45</b>

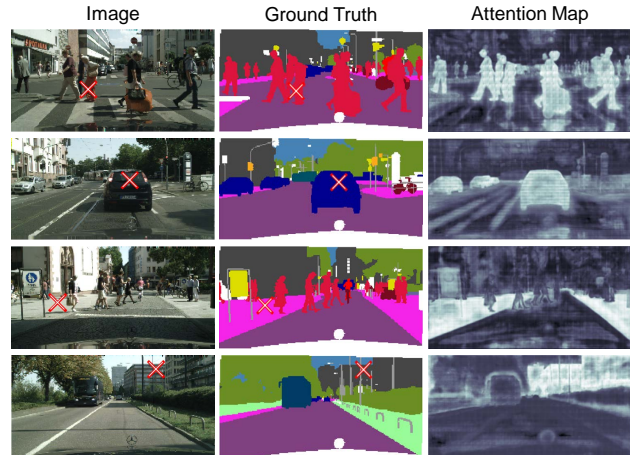


Figure 8. Visualization of attention maps learned with our approach on the validation set of Cityscapes. We present an input image, the ground truth label map and attention map for the pixel marked by red cross in each row.

predicted with our approach and the baseline in Figure 6. The first two rows show the examples from the validation set of Cityscapes and the other two rows show the examples from the validation set of ADE20K. It can be seen that our method produces better segmentation maps compared with the baseline. We mark all the improved regions with white dashed boxes.

Second, inspired by the recent [53], we also visualize the attention maps learned with our approach on the validation set of Cityscapes in Figure 8. For each row, we randomly select a pixel (marked by red cross) in the image and visualize its attention map learned with our approach. It can be seen that our approach also pays more attention to the pixels that belong to same category as the chosen pixel, which is similar to the observation of [53].

Last, we visualize the object detection and instance segmentation results of our approach and the Mask-RCNN on the validation set of COCO in Figure 7. It can be seen that our approach improves the Mask-RCNN consistently on all the examples. For example, the Mask-RCNN fails to detect multiple cars in the last example while our approach achieves better detection performance.

## 5. Conclusion

In this work, we have presented the interlaced sparse self-attention mechanism to improve the efficiency of self-attention scheme. The main idea of our approach is very clear and simple: factoring the dense affinity matrix as the product of two sparse affinity matrices. Especially, our approach is easy to implement based on the existing implementation for self-attention scheme. We empirically compare our approach with various existing approaches and show that our approach achieves competitive performance on various semantic segmentation datasets while being much more efficient compared with the conventional self-attention mechanism.

## References

- [1] [https://en.wikipedia.org/wiki/Interlacing\\_\(bitmaps\)](https://en.wikipedia.org/wiki/Interlacing_(bitmaps)). 2
- [2] H. Caesar, J. Uijlings, and V. Ferrari. Coco-stuff: Thing and stuff classes in context. In *CVPR*, 2018. 5
- [3] L.-C. Chen, G. Papandreou, I. Kokkinos, K. Murphy, and A. L. Yuille. Semantic image segmentation with deep convolutional nets and fully connected crfs. In *ICLR*, 2015. 6
- [4] L.-C. Chen, G. Papandreou, I. Kokkinos, K. Murphy, and A. L. Yuille. Deeplab: Semantic image segmentation with deep convolutional nets, atrous convolution, and fully connected crfs. *PAMI*, 2018. 5, 6
- [5] L.-C. Chen, G. Papandreou, F. Schroff, and H. Adam. Rethinking atrous convolution for semantic image segmentation. *arXiv:1706.05587*, 2017. 5, 6
- [6] Y. Chen, Y. Kalantidis, J. Li, S. Yan, and J. Feng. A<sup>2</sup>-nets: Double attention networks. In *NIPS*, 2018. 2
- [7] R. Child, S. Gray, A. Radford, and I. Sutskever. Generating long sequences with sparse transformers. *arXiv:1904.10509*, 2019. 3
- [8] M. Cordts, M. Omran, S. Ramos, T. Rehfeld, M. Enzweiler, R. Benenson, U. Franke, S. Roth, and B. Schiele. The cityscapes dataset for semantic urban scene understanding. In *CVPR*, 2016. 5
- [9] H. Ding, X. Jiang, B. Shuai, A. Q. Liu, and G. Wang. Context contrasted feature and gated multi-scale aggregation for scene segmentation. In *CVPR*, 2018. 6, 7
- [10] H. Ding, X. Jiang, B. Shuai, A. Q. Liu, and G. Wang. Semantic correlation promoted shape-variant context for segmentation. In *CVPR*, 2019. 6, 7
- [11] M. Everingham, L. Van Gool, C. K. Williams, J. Winn, and A. Zisserman. The pascal visual object classes (voc) challenge. *IJCV*, 2010. 5
- [12] J. Fu, J. Liu, H. Tian, Z. Fang, and H. Lu. Dual attention network for scene segmentation. In *CVPR*, 2019. 1, 2, 5, 6, 7, 8, 9
- [13] K. Gong, X. Liang, D. Zhang, X. Shen, and L. Lin. Look into person: Self-supervised structure-sensitive learning and a new benchmark for human parsing. In *CVPR*, 2017. 6
- [14] K. He, G. Gkioxari, P. Dollár, and R. B. Girshick. Mask R-CNN. In *ICCV*, 2017. 5, 7, 8
- [15] H. Hu, J. Gu, Z. Zhang, J. Dai, and Y. Wei. Relation networks for object detection. In *CVPR*, 2018. 2
- [16] Z. Huang, X. Wang, L. Huang, C. Huang, Y. Wei, and W. Liu. Ccnet: Criss-cross attention for semantic segmentation. In *ICCV*, 2019. 2, 9
- [17] T.-W. Ke, J.-J. Hwang, Z. Liu, and S. X. Yu. Adaptive affinity fields for semantic segmentation. In *ECCV*, 2018. 5, 6
- [18] S. Kong and C. C. Fowlkes. Recurrent scene parsing with perspective understanding in the loop. In *CVPR*, 2018. 6
- [19] Y. Li and A. Gupta. Beyond grids: Learning graph representations for visual recognition. In *NIPS*, 2018. 2, 6
- [20] X. Liang, K. Gong, X. Shen, and L. Lin. Look into person: Joint body parsing & pose estimation network and a new benchmark. *PAMI*, 2018. 5, 6
- [21] X. Liang, Z. Hu, H. Zhang, L. Lin, and E. P. Xing. Symbolic graph reasoning meets convolutions. In *NIPS*, 2018. 2, 6
- [22] X. Liang, H. Zhou, and E. Xing. Dynamic-structured semantic propagation network. In *CVPR*, 2018. 6
- [23] X. Liao, L. He, and Z. Yang. Video-based person re-identification via 3d convolutional networks and non-local attention. *arXiv:1807.05073*, 2018. 1
- [24] G. Lin, A. Milan, C. Shen, and I. D. Reid. Refinenet: Multi-path refinement networks for high-resolution semantic segmentation. In *CVPR*, 2017. 6, 7
- [25] T. Lin, P. Dollár, R. B. Girshick, K. He, B. Hariharan, and S. J. Belongie. Feature pyramid networks for object detection. In *CVPR*, 2017. 7
- [26] T.-Y. Lin, M. Maire, S. Belongie, J. Hays, P. Perona, D. Ramanan, P. Dollár, and C. L. Zitnick. Microsoft coco: Common objects in context. In *ECCV*, 2014. 5, 6
- [27] T. Liu, T. Ruan, Z. Huang, Y. Wei, S. Wei, Y. Zhao, and T. Huang. Devil in the details: Towards accurate single and multiple human parsing. *arXiv:1809.05996*, 2018. 5, 6, 8
- [28] Z. Liu, X. Li, P. Luo, C.-C. Loy, and X. Tang. Semantic image segmentation via deep parsing network. In *ICCV*, 2015. 6
- [29] J. Long, E. Shelhamer, and T. Darrell. Fully convolutional networks for semantic segmentation. In *CVPR*, 2015. 5, 6, 7
- [30] Y. Luo, Z. Zheng, L. Zheng, G. Tao, Y. Junqing, and Y. Yang. Macro-micro adversarial network for human parsing. In *ECCV*, 2018. 6
- [31] N. Ma, X. Zhang, H.-T. Zheng, and J. Sun. Shufflenet v2: Practical guidelines for efficient cnn architecture design. In *ECCV*, 2018. 2
- [32] F. Massa and R. Girshick. maskrcnn-benchmark: Fast, modular reference implementation of Instance Segmentation and Object Detection algorithms in PyTorch. <https://github.com/facebookresearch/maskrcnn-benchmark>, 2018. 7
- [33] R. Mottaghi, X. Chen, X. Liu, N.-G. Cho, S.-W. Lee, S. Fidler, R. Urtasun, and A. Yuille. The role of context for object detection and semantic segmentation in the wild. In *CVPR*, 2014. 5
- [34] X. Nie, J. Feng, and S. Yan. Mutual learning to adapt for joint human parsing and pose estimation. In *ECCV*, 2018. 6
- [35] S. Rota Bul, L. Porzi, and P. Kotschieder. In-place activated batchnorm for memory-optimized training of dnns. In *CVPR*, 2018. 5

- [36] M. S. M. Sajjadi, R. Vemulapalli, and M. Brown. Frame-recurrent video super-resolution. In *CVPR*, 2018. 2
- [37] Z. Shen, M. Zhang, S. Yi, J. Yan, and H. Zhao. Factorized attention: Self-attention with linear complexities. *arXiv:1812.01243*, 2018. 1
- [38] W. Shi, J. Caballero, F. Huszar, J. Totz, A. P. Aitken, R. Bishop, D. Rueckert, and Z. Wang. Real-time single image and video super-resolution using an efficient sub-pixel convolutional neural network. In *CVPR*, 2016. 2
- [39] B. Shuai, Z. Zuo, B. Wang, and G. Wang. Scene segmentation with dag-recurrent neural networks. *PAMI*, 2017. 7
- [40] K. Sun, M. Li, D. Liu, and J. Wang. Igc3: Interleaved low-rank group convolutions for efficient deep neural networks. *arXiv:1806.00178*, 2018. 2
- [41] A. Vaswani, N. Shazeer, N. Parmar, J. Uszkoreit, L. Jones, A. N. Gomez, Ł. Kaiser, and I. Polosukhin. Attention is all you need. In *NIPS*, 2017. 1, 2, 3, 5, 9
- [42] C. Wah, S. Branson, P. Welinder, P. Perona, and S. Belongie. The Caltech-UCSD Birds-200-2011 Dataset. Technical report, 2011. 8
- [43] P. Wang, P. Chen, Y. Yuan, D. Liu, Z. Huang, X. Hou, and G. Cottrell. Understanding convolution for semantic segmentation. In *WACV*, 2018. 6
- [44] X. Wang, R. Girshick, A. Gupta, and K. He. Non-local neural networks. In *CVPR*, 2018. 1, 2, 4, 5, 7, 8, 9
- [45] T. Wu, S. Tang, R. Zhang, J. Cao, and J. Li. Tree-structured kronecker convolutional network for semantic segmentation. *arXiv:1812.04945*, 2018. 6
- [46] T. Xiao, Y. Liu, B. Zhou, Y. Jiang, and J. Sun. Unified perceptual parsing for scene understanding. In *ECCV*, 2018. 6
- [47] G. Xie, J. Wang, T. Zhang, J. Lai, R. Hong, and G.-J. Qi. Igc2: Interleaved structured sparse convolutional neural networks. *arXiv:1804.06202*, 2018. 2
- [48] M. Yang, K. Yu, C. Zhang, Z. Li, and K. Yang. Denseaspp for semantic segmentation in street scenes. In *CVPR*, 2018. 6
- [49] T.-J. Yang, M. D. Collins, Y. Zhu, J.-J. Hwang, T. Liu, X. Zhang, V. Sze, G. Papandreou, and L.-C. Chen. Deep-erlab: Single-shot image parser. *arXiv:1902.05093*, 2019. 2
- [50] C. Yu, J. Wang, C. Peng, C. Gao, G. Yu, and N. Sang. Bisenet: Bilateral segmentation network for real-time semantic segmentation. In *ECCV*, 2018. 6
- [51] C. Yu, J. Wang, C. Peng, C. Gao, G. Yu, and N. Sang. Learning a discriminative feature network for semantic segmentation. In *CVPR*, 2018. 6
- [52] K. Yue, M. Sun, Y. Yuan, F. Zhou, E. Ding, and F. Xu. Compact generalized non-local network. In *NIPS*, 2018. 2, 8, 9
- [53] Y. Yuhui and J. Wang. Ocnet: Object context network for scene parsing. *arXiv:1809.00916*, 2018. 1, 2, 4, 5, 8, 9
- [54] D.-Q. Zhang. clcnnet: Improving the efficiency of convolutional neural network using channel local convolutions. In *CVPR*, 2018. 2
- [55] H. Zhang, K. Dana, J. Shi, Z. Zhang, X. Wang, A. Tyagi, and A. Agrawal. Context encoding for semantic segmentation. In *CVPR*, 2018. 5, 6
- [56] H. Zhang, H. Zhang, C. Wang, and J. Xie. Co-occurrent features in semantic segmentation. In *CVPR*, 2019. 1, 2, 8
- [57] R. Zhang, S. Tang, Y. Zhang, J. Li, and S. Yan. Scale-adaptive convolutions for scene parsing. In *ICCV*, 2017. 6
- [58] T. Zhang, G.-J. Qi, B. Xiao, and J. Wang. Interleaved group convolutions. In *ICCV*, 2017. 2
- [59] X. Zhang, X. Zhou, M. Lin, and J. Sun. Shufflenet: An extremely efficient convolutional neural network for mobile devices. *CVPR*, 2018. 2
- [60] H. Zhao, J. Shi, X. Qi, X. Wang, and J. Jia. Pyramid scene parsing network. In *CVPR*, 2017. 5, 6, 8, 9
- [61] H. Zhao, Z. Yi, L. Shu, S. Jianping, C. C. Loy, L. Dahua, and J. Jia. Ppsnet: Point-wise spatial attention network for scene parsing. In *ECCV*, 2018. 6
- [62] B. Zhou, H. Zhao, X. Puig, S. Fidler, A. Barriuso, and A. Torralba. Scene parsing through ade20k dataset. In *CVPR*, 2017. 5
- [63] Z. Zhou, M. M. R. Siddiquee, N. Tajbakhsh, and J. Liang. Unet++: A nested u-net architecture for medical image segmentation. In *MICCAI*, 2018. 6